

Model for anaphase B: Role of three mitotic motors in a switch from poleward flux to spindle elongation

I. Brust-Mascher, G. Civelekoglu-Scholey, M. Kwon, A. Mogilner, and J. M. Scholey*

Laboratory of Cell and Computational Biology, Center for Genetics and Development, University of California, Davis, CA 95616

Communicated by J. Richard McIntosh, University of Colorado, Boulder, CO, September 27, 2004 (received for review July 9, 2004)

It has been proposed that the suppression of poleward flux within interpolar microtubule (ipMT) bundles of *Drosophila* embryonic spindles couples outward forces generated by a sliding filament mechanism to anaphase spindle elongation. Here, we (*i*) propose a molecular mechanism in which the bipolar kinesin KLP61F persistently slides dynamically unstable ipMTs outward, the MT depolymerase KLP10A acts at the poles to convert ipMT sliding to flux, and the chromokinesin KLP3A inhibits the depolymerase to suppress flux, thereby coupling ipMT sliding to spindle elongation; (*ii*) used KLP3A inhibitors to interfere with the coupling process, which revealed an inverse linear relation between the rates of flux and elongation, supporting the proposed mechanism and demonstrating that the suppression of flux controls both the rate and onset of spindle elongation; and (*iii*) developed a mathematical model using force balance and rate equations to describe how motors sliding the highly dynamic ipMTs apart can drive spindle elongation at a steady rate determined by the extent of suppression of flux.

Chromosome segregation depends upon the action of the spindle, a protein machine that uses ensembles of kinesin and dynein motors plus microtubule (MT) dynamics to move chromatids polewards (anaphase A) and to elongate the spindle (anaphase B) (1). Anaphase B is driven in part by a bipolar kinesin-dependent sliding filament mechanism (2–9), with the extent of spindle elongation determined by MT polymerization in the overlap zone (2). Poleward flux, the movement of tubulin subunits from the MT plus ends facing the spindle equator to their minus ends at the poles (10–14), is proposed to constrain the length of metaphase spindles, with subsequent inhibition of depolymerization at the poles converting metaphase flux to anaphase spindle elongation (12, 15, 16).

In support of this hypothesis, we observed that a suppression of poleward flux occurs at anaphase B onset: tubulin speckles within interpolar MTs (ipMTs) of *Drosophila* embryonic spindles fluxed toward the stationary poles of preanaphase B (herein meaning metaphase–anaphase A) spindles, but during anaphase B the speckles moved apart at the same rate as the poles (12). Here, we propose that three mitotic motors play critical roles in this process, based on previous studies (Fig. 1*A*). First, the bipolar kinesin KLP61F drives a sliding filament mechanism that underlies spindle elongation, because inhibiting KLP61F (in an Ncd-null mutant to circumvent the collapse of prometaphase spindles) inhibits anaphase B (9). Second, the kin I kinesin KLP10A depolymerizes ipMTs at the poles of preanaphase spindles, converting sliding to poleward flux; its inhibition leads to the premature suppression of flux and spindle elongation (14), suggesting that it is down-regulated at the onset of anaphase B. Finally, the chromokinesin KLP3A organizes ipMTs into bundles and is required for efficient anaphase spindle elongation (17).

Here, we report experimental and theoretical results that provide a quantitative description of anaphase B dynamics in terms of these molecular mechanisms and reveal that the rate of anaphase spindle elongation is determined by (*i*) the unloaded rate of ipMT sliding and (*ii*) the extent of reduction of ipMT depolymerization at the poles.

Materials and Methods

***Drosophila* Stocks and Embryo Preparation.** Flies were maintained and 0- to 2-h embryos were collected as described (9, 17). Embryos expressing GFP::tubulin were provided by Allan Spradling (Carnegie Institution, Washington, DC). Embryos were microinjected with rhodamine-conjugated bovine tubulin (Cytoskeleton, Denver), allowed to recover for 5 min, and microinjected with affinity-purified anti-KLP3A tail antibodies or purified recombinant KLP3A stalk proteins at concentrations ranging from 20 to 30 mg/ml (17). Control embryos were injected with identical concentrations of preimmune IgG or rabbit IgG (Sigma) or GST proteins.

Fluorescent Speckle Microscopy (FSM) and 3D Reconstructions. MT flux was imaged and measured as described (12), by using an Olympus (Melville, NY) microscope equipped with an Ultra-View spinning disk confocal head (Perkin–Elmer) and a 100× 1.35-numerical aperture objective with a time interval of 1.5 sec. Images were analyzed by using METAMORPH IMAGING software (Universal Imaging, West Chester, PA). Kymography was used to quantify speckle movement. Calculations and statistical analyses were done on Microsoft EXCEL. For 3D reconstructions, embryos were injected with rhodamine tubulin, and z-stacks were acquired at 0.2- μ m steps. The stacks were deconvolved, and projections and cross sections were generated by using AUTOVISUALIZE and AUTODEBLUR (AutoQuant Imaging, Watervliet, NY).

Fluorescence Recovery After Photobleaching (FRAP). Embryos expressing GFP-tubulin were imaged on a Zeiss 510 Meta confocal microscope with a 63× 1.40-numerical aperture objective at 23°C. Areas of 12–20 μ m² in the center of the spindle were bleached and time-lapse images were acquired. Total fluorescence intensity in the bleached area was measured as a function of time and fit to an exponential recovery by using KALEIDAGRAPH (Synergy Software, Reading, PA).

Computational Modeling Methods. We used random number generators to simulate the initial ipMT configurations and fluctuations in polymerization/depolymerization rates. The explicit Euler method [in MATLAB (Mathworks, Natick, MA)] was used to solve the equations of motion for the ipMTs on a desktop computer.

Supporting Information. *Supporting Text*, which provides details of the calculations, and movies of computer simulations are available as supporting information, which is published on the PNAS web site.

Results

Experimental Results. *The rates of poleward flux and anaphase spindle elongation are inversely related.* We examined the relationship among poleward flux, ipMT sliding, and spindle length in

Freely available online through the PNAS open access option.

Abbreviations: FSM, fluorescent speckle microscopy; FRAP, fluorescence recovery after photobleaching; MT, microtubule; ipMT, interpolar MT.

*To whom correspondence should be addressed. E-mail: jmscholey@ucdavis.edu.

© 2004 by The National Academy of Sciences of the USA

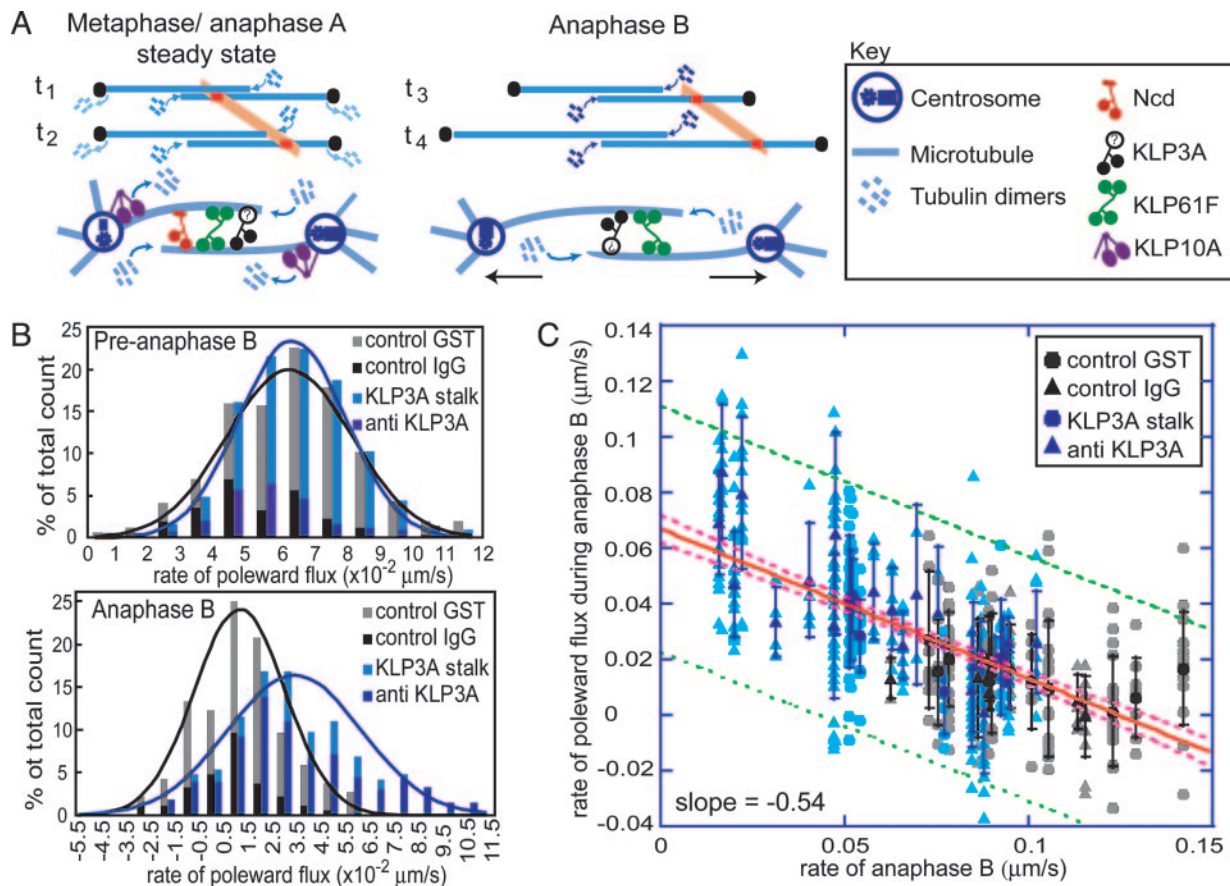


Fig. 1. Qualitative model for anaphase B and experimental test of the model. (A) Dynamics of spindle poles (black dots), ipMTs (overlapping blue lines) that add or lose tubulin subunits (blue), and tubulin speckles (orange) at time points t₁ and t₂ (preanaphase B) and t₃ and t₄ (anaphase B). In preanaphase B, pole–pole spacing remains constant, and opposite end assembly/disassembly is associated with poleward flux (orange). In anaphase B, depolymerization at the poles ceases, and ipMT sliding drives pole–pole separation; thus, speckles move away from the equator at the same rate as the poles. In the molecular model of anaphase B, the turning off of depolymerization at the poles by inhibiting KLP10A allows KLP61F-driven ipMT sliding to push the poles apart. KLP3A organizes ipMTs into bundles, whereas the braking action of Ncd is turned off before anaphase B onset. (B) Histograms of the rates of flux in preanaphase B (Upper) and anaphase B (Lower) spindles in control (gray) and KLP3A-inhibited (blue) embryos. The number of counts was normalized to the total number. Note that there are large variations in the flux rate, and when the mean is near zero, some values are negative. (C) During anaphase B, the rates of poleward flux and spindle elongation are linearly inversely related. Data points display the behavior of individual fluorescent tubulin speckles within individual spindles of control (gray) and KLP3A-inhibited (blue) embryos; darker symbols represent the mean for each spindle. The red line is the best fit to the data; the pink and green dashed lines are the 95% confidence intervals for the best fit line and data points, respectively.

Drosophila embryos. Plots of spindle pole separation versus time (Fig. 2A) reveal that the preanaphase B spindle maintains a constant length, and FSM (18) shows that tubulin speckles flux persistently poleward within ipMT bundles (Fig. 2B). During anaphase B, the spindle elongates at a linear rate (Fig. 2A), and speckles move away from the equator at the same rate as the poles, consistent with ipMT sliding (Fig. 2B). To explain these dynamic events, we hypothesized that the suppression of flux couples ipMT sliding to spindle elongation (Fig. 1A).

We were able to test this hypothesis by microinjecting embryos with antibody and dominant negative protein inhibitors of the chromokinesin KLP3A, which interfere with spindle elongation during anaphase (17). These inhibitors have no effect on the rates of poleward flux during preanaphase B but surprisingly cause poleward flux to persist after anaphase B onset (Table 1 and Fig. 1B), suggesting that inhibiting KLP3A somehow inhibits the down-regulation of ipMT depolymerization at the poles that normally occurs at anaphase B onset. These experiments reveal that the rate of poleward flux within ipMT bundles displays an inverse linear relation with the rate of pole–pole separation (Fig. 1C), so that low flux rates correlate with high anaphase B rates. This provides evidence that the suppression of poleward flux

within ipMT bundles (plausibly resulting from a loss of KLP10A activity) couples ipMT sliding to spindle elongation, thereby controlling the onset and rate of anaphase B.

Dynamics of ipMTs in the central spindle. 3D reconstructions of deconvolved spinning disk confocal images (Fig. 2C) reveal approximately nine robust-looking ipMT bundles in a *Drosophila* embryonic spindle. Previous electron microscopies (8) reveal that these ipMT bundles, which are not highly ordered, have an average overlap of ≈ 1 μm in early anaphase B and contain ≈ 30 MTs per bundle per half spindle. We used FRAP to study the dynamics of these ipMTs in the anaphase B central spindle and observed a surprisingly rapid recovery of GFP::tubulin fluorescence (Fig. 2D; recovery half time of a 2- μm bleach zone was 3–6 sec). This recovery is much faster than observed in other systems (19) but is an order of magnitude slower than the characteristic diffusion time of free tubulin dimers, assuming a diffusion coefficient of ≈ 8 $\mu\text{m}^2/\text{sec}$ (20), and presumably reflects turnover due to dynamic instability of ipMT plus ends displaying overall growth, combined with the poleward translocation of bleached and unbleached ipMT segments into and out of the bleach zone, in accordance with FSM data (Fig. 2B). How does such a dynamic array of ipMTs elongate the spindle at the steady linear rate observed?

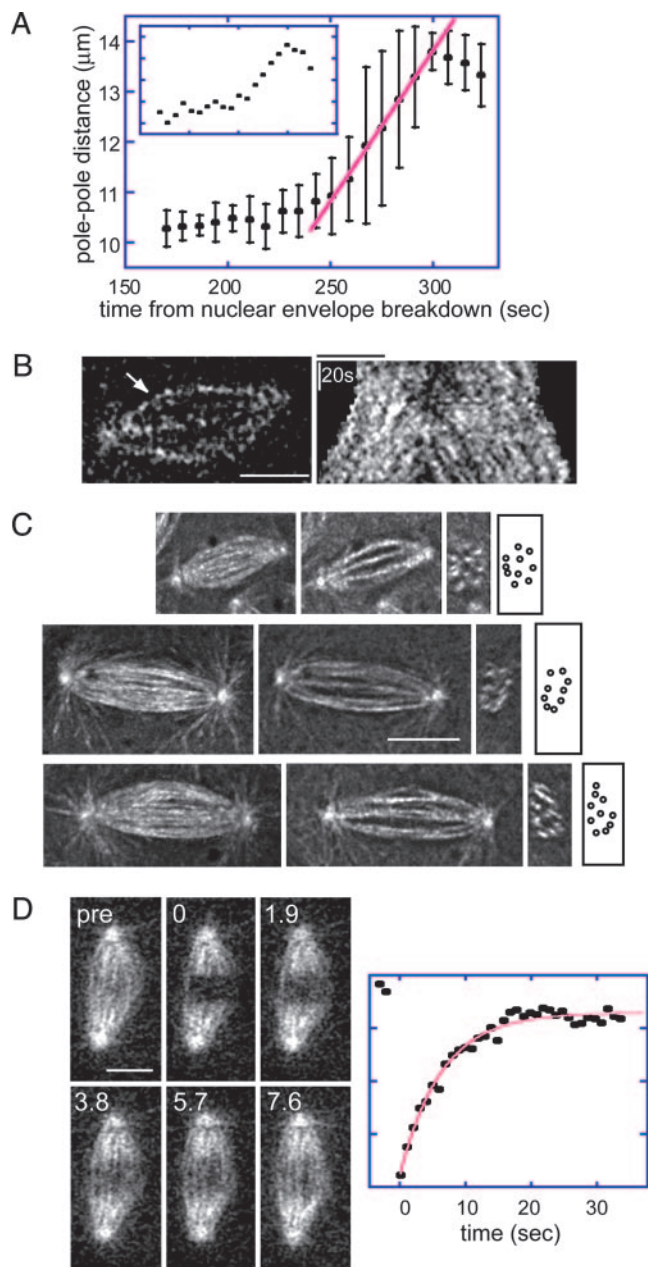


Fig. 2. Organization and dynamics of ipMT bundles in *Drosophila* embryonic anaphase B spindles. (A) Pole–pole separation versus time during preanaphase B (160–250 sec) and anaphase B (250–300 sec). Spindle elongation is linear. Main graph, average data from multiple spindles; the standard deviation arises from variations in the linear rate between different spindles. (Inset) Typical spindle. Red line, regression line fit to the mean. (B) FSM of ipMT bundles. The kymograph (Right) during preanaphase B and anaphase B [for the bundle indicated by the arrow (Left) during anaphase B] shows that tubulin speckles flux away from the equator throughout. (C) ipMTs. Longitudinal projections (Left), XY sections (Center Left), transverse sections (Center Right), and cartoons of transverse sections (Right) reveal approximately nine ipMT bundles per spindle. (D) MT turnover determined by FRAP. Micrographs of a spindle before (pre) and after (time in seconds) photobleaching (Left) and the plot of fluorescence intensity (arbitrary units) versus time after photobleaching (Right) reveal that tubulin turnover in the central spindle is fast (recovery half time of 4.5 sec in this example). (Bar, 5 μm .)

Mathematical Model for Anaphase Spindle Elongation. We developed a model to address the above question, to provide a quantitative description of anaphase B dynamics in terms of the underlying molecular events, and to identify testable predictions.

Table 1. Poleward flux during the preanaphase B steady state and anaphase B

	Preanaphase B flux, $\mu\text{m/s}$	Anaphase B poleward flux, $\mu\text{m/s}$
Control IgG	0.053 ± 0.017 (93/13/3)	0.008 ± 0.016 (51/8/3)
Anti-KLP3A	0.055 ± 0.016 (107/19/5)	0.035 ± 0.030 (258/30/6)
Control GST	0.066 ± 0.021 (295/12/2)	0.014 ± 0.020 (136/11/2)
KLP3A stalk	0.066 ± 0.017 (365/18/3)	0.034 ± 0.021 (83/7/3)

Parentheses indicate the number of speckles, spindles, and embryos, respectively, that were analyzed.

Model definitions and assumptions. (i) The state variables, $S(t)$ and $L(t)$, are pole–pole and ipMT overlap distances at time t , respectively (Fig. 3A), and their time derivatives are the rate of change of these distances. (ii) $V_{\text{sliding}}(t)$ denotes the time-dependent rate of sliding apart of ipMTs, which, we propose, corresponds to the observed rate of speckle movement away from the spindle equator. We assume that each sliding motor is characterized by a linear force–velocity relationship (ref. 21; Fig. 5, which is published as supporting information on the PNAS web site) that the action of multiple motors is linearly additive, and that the number of force-generating motors is proportional to the overlap length $L(t)$. We assume that the sliding motors work against an effective viscous drag imposed by the separating spindle poles (effective drag coefficient, μ). (iii) V_{depoly}^- is the average rate of depolymerization of ipMT minus ends, which, we propose, corresponds to the flux rate. In the model, we assume that ipMT minus end depolymerization is confined to the poles and does not occur in the spindle itself. V_{poly}^+ is the mean rate of polymerization of the dynamic plus ends of ipMTs, determined by dynamic instability parameters. (iv) The validity of the quantitative model presented below is independent of the iden-

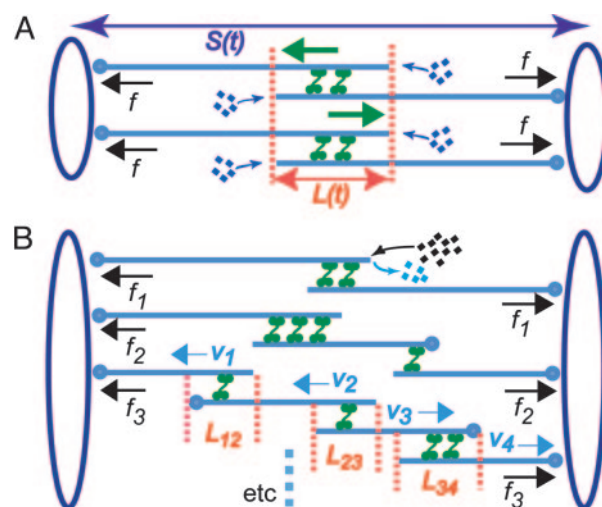


Fig. 3. Model spindle geometry. (A) A simplified spindle with two identical arrays of ipMTs, each composed of two overlapping antiparallel MTs. Here, ipMTs have the same overlap, and their plus ends polymerize at the same rate. $S(t)$ is the pole–pole distance, and $L(t)$ is the length of the ipMT overlap. Green arrows indicate sliding of ipMTs by bipolar motors; black arrows indicate the motor-generated forces, equal to f for both ipMT arrays. (B) A realistic spindle with ipMT arrays composed of two, three, and four overlapping MTs. In the lower ipMT array, the overlap length between the parallel (L_{12} and L_{34}) and antiparallel (L_{23}) MTs and the sliding velocity of each MT (V_1 , V_2 , V_3 , and V_4) are indicated. The dynamic instability of the plus ends, resulting in an average net polymerization, is shown only for the left MT in the top ipMT array. Forces generated by bipolar motors in different ipMT arrays (e.g., f_1 , f_2 , and f_3) are different.

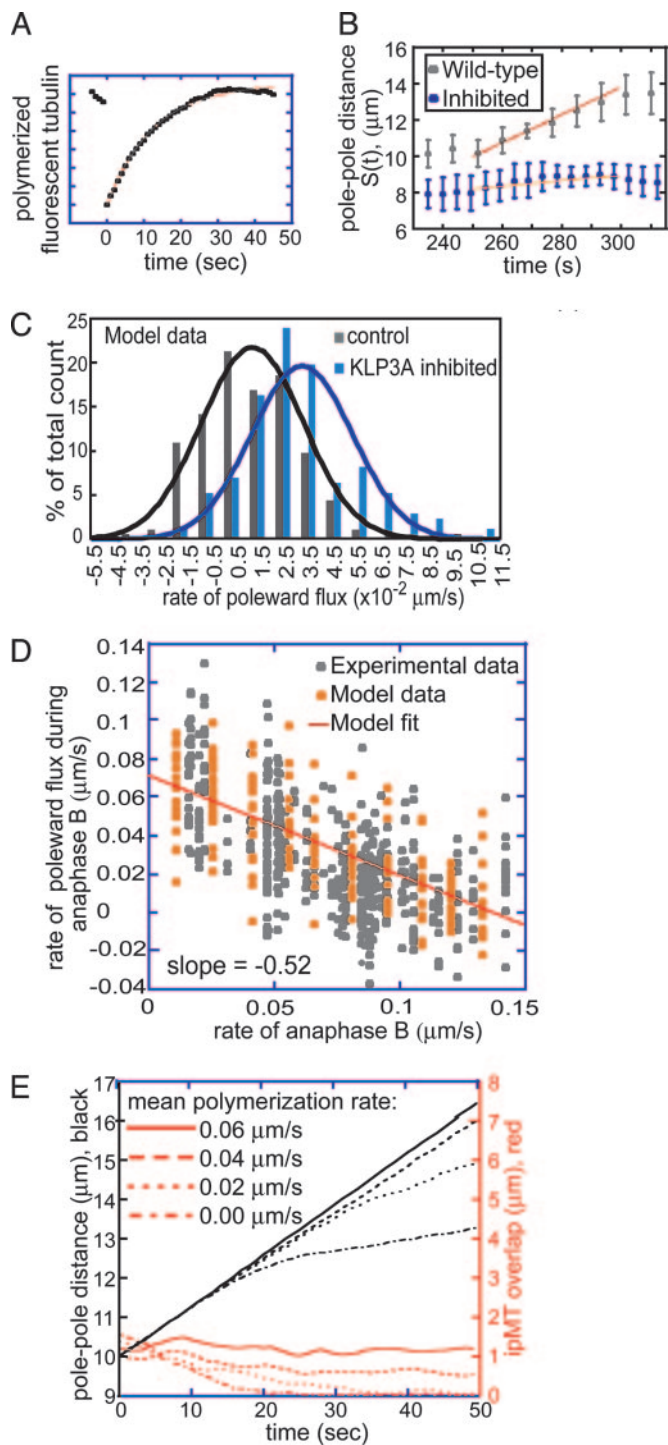


Fig. 4. Model results. (A) FRAP simulation. $V_{\text{depoly}}^- = 0 \mu\text{m}/\text{sec}$. (B) Experimental and theoretical plots of pole–pole separation [$S(t)$] versus time during anaphase B. Control (gray) and KLP3A-inhibited (blue) data and theoretical curves (red, control; orange, KLP3A-inhibited). $V_{\text{depoly}}^- = 0.015$ and $0.055 \mu\text{m}/\text{sec}$ for control and KLP3A-inhibited embryos, respectively. (C) Histograms of the rates of flux in anaphase B in control (gray) and KLP3A-inhibited embryos (blue) obtained by numerical solutions. $V_{\text{depoly}}^- = 0 - 0.03$ and $0.02 - 0.07 \mu\text{m}/\text{sec}$ for control and KLP3A-inhibited embryos, respectively. The flux rate exhibits large variances similar to the experimental data (Fig. 1B). (D) Numerical results for the flux and spindle elongation rates in spindles where V_{depoly}^- alone has been varied ($V_{\text{depoly}}^- = 0 - 0.07 \mu\text{m}/\text{sec}$). The model solutions (orange) are superimposed on the data from Fig. 1C (gray). (E) Plots of pole–pole distance [$S(t)$, black] and ipMT overlap [$L(t)$, red] for various rates of V_{poly}^+ . During the first half of anaphase B, the poles separate steadily at a

the central spindle and yields recovery kinetics in good agreement with the experimental FRAP data (Fig. 4A).

The solutions to the model equations displayed as graphs of $S(t)$ versus time, histograms, and anaphase B–flux rate relationship (Fig. 4) were all in good agreement with the experimental data, supporting the idea that our molecular model can account for anaphase B dynamics. Plots of $S(t)$ versus time show that, despite the dynamic nature of the overlap zone and the increase in load as the poles start moving at anaphase B onset, KLP61F motors continue to work in the “unloaded” regime throughout (see *Supporting Text*) and are capable of sliding apart ipMTs and elongating the spindle at a steady linear rate (Fig. 4B). This rate is determined only by the unloaded rate of KLP61F-driven sliding and the extent of suppression of flux (Fig. 4D).

Variations of up to an order of magnitude in other model parameters, e.g., the maximal motor force, number of ipMTs, number of motors, viscous drag, dynamic instability of ipMT plus ends, and the mean ipMT plus end polymerization rate, as well as deviations from linearity in the force–velocity curves, have no significant effect on the rate of spindle elongation, at least initially. Fig. 4E, for example, shows that reasonable values of the mean ipMT plus end polymerization rate (V_{poly}^+) support a steady, linear rate of pole–pole separation throughout anaphase B. However, decreasing the polymerization rate does influence the spindle elongation rate during the second half of anaphase B (>25 sec), but in the embryo this could be compensated by the pulling activity of cortical dynein (14). Note that, even when the mean polymerization rate is zero, the spindle can elongate, albeit at a reduced rate, plausibly due to KLP61F (now working close to stall), pushing apart those ipMTs that happen to be growing (*Supporting Text*). Consequently, under conditions of low V_{poly}^+ , a small increase in the drag or any other external load should slow down KLP61F-driven spindle elongation.

Discussion

This work provides a quantitative description of the observed dynamics of anaphase spindle elongation in terms of a simple molecular mechanism (Fig. 1A), in which the ipMTs are slid apart by KLP61F motors plausibly working close to their free sliding rate, in both the elongating spindle and the preanaphase spindle. Remarkably, despite the dynamic, somewhat disorganized nature of the ipMTs, the sliding motors can develop a total force an order of magnitude greater than the characteristic viscous resistance to spindle pole movement, enabling them to drive steady, linear spindle elongation. The rate at which the persistently sliding ipMTs elongate the spindle depends on the extent of suppression of KLP10A activity, and KLP3A plays an unexpected coupling role in the switch from poleward flux to spindle elongation.

Predictions of the Model. The model predicts that experimentally perturbing the mean ipMT growth rate or increasing the drag force up to an order of magnitude should not affect the rate of spindle elongation, but changing the unloaded sliding velocity of KLP61F motors should. The idea that KLP61F slides ipMTs at a constant velocity throughout predicts that it contributes to poleward flux within ipMTs, and an obvious prediction of our model is that KLP10A is down-regulated at anaphase B onset. Finally, the model predicts that when $V_{\text{sliding}} = 0$, and spindle

velocity independent of the polymerization rate (V_{poly}^+). However, the ipMT overlap is affected by V_{poly}^+ . Note the small fluctuations in $L(t)$ due to dynamic instability. The catastrophe frequency was varied as 0.04, 0.08, 0.16, and 0.2/sec to yield the indicated polymerization rates. $V_{\text{depoly}}^- = 0 \mu\text{m}/\text{sec}$. The initial average overlap is $1-1.5 \mu\text{m}$, $n = 30$, $f_{\text{rescue}} = 0.2/\text{sec}$, and $f_{\text{catastrophe}} = 0.02/\text{sec}$, unless indicated otherwise. All unspecified parameter values are given in Table 2.

length does not change, there should be no flux. These predictions are under investigation.

Role of KLP3A. KLP3A appears to couple ipMT sliding to spindle elongation by a mechanism more complex than simply facilitating KLP61F-driven sliding (17). We propose that, by organizing ipMTs into robust bundles, it influences the critical ratio of active KLP10A to ipMT minus ends at the poles. In controls, this ratio decreases substantially at anaphase B onset, when some hypothetical signal turns off KLP10A activity, so depolymerization is suppressed and the spindle elongates. In KLP3A-inhibited embryos, ipMT bundles are disorganized, and fewer minus ends are focused at the poles. In preanaphase B spindles, the rate of depolymerization remains at control levels, because the rate at which ipMTs are slid and fed into the poles is limiting, but at anaphase B onset, the ratio of residual KLP10A to ipMT ends remains high, allowing depolymerization and flux to persist, inhibiting spindle elongation. Although this remains to be tested experimentally, computer simulations using varying ratios of KLP10A to ipMT minus ends support the hypothesis (see Fig. 6, which is published as supporting information on the PNAS web site).

Variance in the Flux Rates. On individual spindles, we observed high variance in the rates of poleward flux (Fig. 1C) but not in the rates of spindle elongation (Fig. 2A Inset), which depends on multiple MTs acting on each pole at once, thus averaging out the variance. A quantitative analysis of the variance in flux rates reveals that it may be due to fluctuations in KLP10A activity and/or Poisson fluctuations in the number of subunits disassembled from the MT minus ends at the poles. Other potential causes, such as tracking errors, velocity variance due to the motor-dependent shearing of parallel MT segments within ipMT bundles (refs. 4 and 8; Fig. 3B), or fluctuations in the rate constants of mechanochemical coupling by the sliding motors, appear insufficient to account for the large variance (see, Supporting Text).

Limitations of the Model. Our model does not address the formation or function of preanaphase B spindles or the contribution of additional mechanisms to anaphase B, e.g., KLP61F sliding ipMTs against a spindle matrix, or dynein/astral MTs pulling the

poles apart (see Movies 6 and 7, which are published as supporting information on the PNAS web site). It does show that, despite the highly dynamic nature of the central spindle, our sliding filament-based model can account for steady anaphase spindle elongation, at least initially, and additional mechanisms are not necessary. However, if there is no ipMT polymerization (V_{poly}^+) at the equator, linear spindle elongation during the second half of anaphase B (Fig. 4E) may require an additional component, plausibly cortical dynein (9).

Implications for the Rate of Mitosis. The *Drosophila* early embryo carries out multiple mitoses very rapidly (cell cycle duration, ≈ 10 min). Accordingly, both anaphase B spindle elongation and anaphase spindle ipMT turnover occur faster than in other systems (e.g., refs. 19 and 22), yet KLP61F motors work at the same slow rate as bipolar kinesins from diverse organisms (23). Based on our data (Figs. 1C, 4D, and Fig. 7, which is published as supporting information on the PNAS web site), we propose that the rate of elongation of different spindles may be governed by the extent of down-regulation of depolymerization at the poles. This would be completely turned off in *Drosophila* embryos, providing maximal coupling and allowing ipMT sliding to drive elongation at the maximum rate, but, in other spindles, the partial down-regulation of flux may produce a slower elongation rate. In contrast, in different muscle fibers, changes in sliding motor activity via changes in the rate of ADP release by myosin II governs the rate of fiber shortening (24).

Conclusion

This model, supported by experimental data, describes the dynamics of anaphase B in terms of a plausible molecular mechanism in which the onset and rate of spindle elongation are controlled by the suppression of poleward flux. The model is an advance toward a quantitative description of mitosis and can be generalized to describe spindle length-determining mechanisms operating elsewhere (25).

Note Added in Proof: KLP61F, KLP10A, and KLP3A are members of the kinesin-5, kinesin-13, and kinesin-4 families, respectively (26).

This work was supported by National Institutes of Health Grants GM-55507 and GM-068952. We thank multiple colleagues and reviewers for help and discussions.

- Scholey, J. M., Brust-Mascher, I. & Mogilner, A. (2003) *Nature* **422**, 746–752.
- Masuda, H., McDonald, K. & Cande, W. Z. (1988) *J. Cell Biol.* **107**, 623–633.
- McIntosh, R. & McDonald, K. L. (1989) *Sci. Am.* **261**, 48–56.
- Mastrorarde, D. N., McDonald, K. L., Ding, R. & McIntosh, J. R. (1993) *J. Cell Biol.* **123**, 1475–1489.
- Hogan, C. J., Wein, H., Wordeman, L., Scholey, J. M., Sawin, K. E. & Cande, W. Z. (1993) *Proc. Natl. Acad. Sci. USA* **90**, 6611–6615.
- Saxton, W. M. & McIntosh, J. R. (1987) *J. Cell Biol.* **105**, 875–886.
- Straight, A. F., Sedat, J. W. & Murray, A. W. (1998) *J. Cell Biol.* **143**, 687–694.
- Sharp, D. J., McDonald, K. L., Brown, H. M., Matthies, H. J., Walczak, C., Vale, R. D., Mitchison, T. J. & Scholey, J. M. (1999) *J. Cell Biol.* **144**, 125–138.
- Sharp, D. J., Brown, H. M., Kwon, M., Rogers, G. C., Holland, G. & Scholey, J. M. (2000) *Mol. Biol. Cell.* **11**, 241–253.
- Mitchison, T. J. (1989) *J. Cell Biol.* **109**, 637–652.
- Mitchison, T. J. & Salmon, E. D. (1992) *J. Cell Biol.* **119**, 569–582.
- Brust-Mascher, I. & Scholey, J. M. (2002) *Mol. Biol. Cell* **13**, 3967–3975.
- Maddox, P., Desai, A., Oegema, K., Mitchison, T. J. & Salmon, E. D. (2002) *Curr. Biol.* **12**, 1670–1674.
- Rogers, G. C., Rogers, S. L., Schwimmer, T. A., Ems-McClung, S. C., Walczak, C. E., Vale, R. D., Scholey, J. M. & Sharp, D. J. (2004) *Nature* **427**, 364–370.
- Margolis, R. L., Wilson, L. & Kiefer, B. I. (1978) *Nature* **272**, 450–452.
- Mitchison, T. J. & Sawin, K. E. (1990) *Cell Motil. Cytoskeleton* **16**, 93–98.
- Kwon, M., Mulia-Morales, S., Brust-Mascher, I., Sharp, D. J., Rogers, G. C. & Scholey, J. M. (2004) *Mol. Biol. Cell.* **15**, 219–233.
- Waterman-Storer, C. M. & Salmon, E. D. (1998) *Biophys. J.* **75**, 2059–2069.
- Saxton, W. M., Stemple, D. L., Leslie, R. J., Salmon, E. D., Zavortink, M., McIntosh, J. R. (1984) *J. Cell Biol.* **99**, 2175–2186.
- Salmon, E. D., Saxton, W. M., Leslie, R. J., Karow, M. L. & McIntosh, J. R. (1984) *J. Cell Biol.* **99**, 2157–2164.
- Schnitzer, M. J., Visscher, K. & Block, S. M. (2000) *Nat. Cell Biol.* **2**, 718–723.
- Cohn, S. A. & Pickett-Heaps, J. (1988) *Eur. J. Cell Biol.* **46**, 523–530.
- Cole, D. G., Saxton, W. M., Sheehan, K. B. & Scholey, J. M. (1994) *J. Biol. Chem.* **269**, 22913–22916.
- Siemenkowski, R. F., Wiseman, M. O. & White, H. D. (1985) *Proc. Natl. Acad. Sci. USA* **82**, 658–662.
- Gaetz, J. & Kapoor, T. M. (2004) *J. Cell Biol.* **165**, 465–471.
- Lawrence, C. J., Dawe, R. K., Christie, K. R., Cleveland, D. W., Dawson, S. C., Endow, S. A., Goldstein, L. S., Goodson, H. V., Hirokawa, N., Howard, J., et al. (2004) *J. Cell Biol.* **167**, 19–22.

Supporting Information

Force-velocity relationship for sliding motors.

We assume that motor heads of the bipolar kinesins are characterized by a linear force-

velocity relation: $f = F_m \left(1 - \frac{v}{V_m}\right)$ (Fig. S1), where v is the velocity of the plus-end-

directed motor movement.

Derivation of the motor generated forces between antiparallel and parallel MTs in ipMT arrays.

Let us first consider two overlapping antiparallel MTs crosslinked by a single motor (as in Fig. 3B upper ipMT array), such that the MTs are moving with velocities $V_{sliding, left} = V_l$ and $V_{sliding, right} = V_r$ with their minus ends leading, to the left and right, respectively. In this configuration, the forces generated by two opposite motor heads are

$$f_l = F_m \left(1 - \frac{v + V_l}{V_m}\right), f_r = F_m \left(1 - \frac{V_r - v}{V_m}\right),$$
 and have to be equal since motor heads are

connected by non-motor domains. Solving this equality we find that $v = \frac{V_r - V_l}{2}$ and

therefore a force $f = F_m \left(1 - \frac{V_l + V_r}{2V_m}\right)$ will be generated by each motor sliding apart two

overlapping antiparallel MTs moving with velocities V_l and V_r . We do not analyze the associated motor transport, because we assume that the motors associate fast with overlap regions between pairs of MTs as they become available (1), therefore the motor transport does not affect the number of engaged motors.

Next, let us consider two parallel MTs crosslinked by a motor, (Fig. 3B, lower ipMT array, the two MTs at left) such that the MTs are moving with velocities V_1 and V_2 (with minus ends leading), respectively. In this configuration, the forces generated by two

opposite motor heads are $f = \pm F_m \left(1 - \frac{v + V_{1,2}}{V_m} \right)$, and have to be equal since motor heads

are connected by non-motor domains. Solving this equality, we find that $v = V_m - \frac{V_1 + V_2}{2}$

and therefore a force of magnitude $f = F_m \frac{V_2 - V_1}{2V_m}$ will be generated by each motor

between two parallel crosslinked MTs, slowing down the faster MT and accelerating the slower one.

Since the force across each ipMT array is constant, in a given ipMT array, the force generated by sliding motors in each overlap is the same, giving rise to equation 6, for example, for the lower ipMT array in Figure 3B.

Computer code.

Describing the kinematic equations for each ipMT array together with the force-balance equation (eqn. 7) results in a large system of coupled differential equations.

A computer code was developed to obtain the numerical solutions and generate simulations displayed as movies. An important part of the code is the random number-generated stochastic variations of the model parameters and initial conditions. There are 9 ipMT bundles per spindle (Fig. 2C), and we assume that each one of these ipMT bundles contains 3-10 ipMT arrays, which in turn, are composed of 2-4 interconnected

MTs stretching between the poles (Fig. 3B). Therefore, in our code, we assume that there are typically 30-90 ipMT arrays composed of varying numbers of MTs per spindle. MTs in each ipMT array interact pair wise, and only one among all MTs facing each pole with their minus end is associated with that pole, while the other(s) are not. In the ipMT arrays composed of 3 MTs (Fig. 3B, middle ipMT array), the ‘middle’ MT which is not associated with either one of the poles overlaps and interacts with the two others, which are associated with the poles and do not overlap nor interact directly with each other. In the ipMT arrays with 4 MTs, the configuration is similar to that shown in Figure 3B, lower ipMT array. The initial position of the MT ends in each ipMT array is computed using random number generators, giving rise to an average antiparallel overlap of $\sim 1 \mu\text{m}$, and an average parallel overlap of $\sim 2.5 \mu\text{m}$.

At each computational step, with Δt corresponding to 1 sec, we solve the kinematic equations for each ipMT array and the force balance equation simultaneously based on the current parallel and antiparallel overlaps between the ipMTs. The force across each ipMT array (f_i , in Fig. 3B) is an unknown variable at each time step. Also, the velocities of individual MTs in each ipMT array (v_i , in Fig. 3B) are unknown, and they are computed at each time step. The total force generated by sliding motors in the spindle is obtained by summing up the force for all ipMT arrays and this is balanced by the drag force acting on the poles.

This leads to a well posed problem of linear algebra which is solved at every time step to find the velocities of all MTs comprising each ipMT array, and the velocity of the spindle poles. The plus and minus ends of individual MTs in each ipMT array are then updated using the newly computed velocities, while all plus ends undergo dynamic instability calculated using the scheme described in Sprague et al. (2), and the minus ends of those MTs associated with the poles are shortened through depolymerization at prescribed rates (stochastic variations superposed on an average rate V_{depoly}^-). Finally, new overlap lengths are computed for the updated configurations and all calculations are repeated at the next step. Parameters are listed in Table S1, and the specific values used are given in the figure legends. Because only orders of magnitude of most model parameters are published, in the simulations, we chose the values giving the best fit to the data (Table S1).

Corresponding simulations demonstrate that the average antiparallel overlap of all ipMT arrays in the central spindle changes slowly, while the antiparallel overlap between individual ipMT arrays whose ends grow/shrink stochastically due to dynamic instability changes rapidly. On the other hand, the average parallel overlap of all ipMT arrays within the same half-spindle increases very fast, while their plus ends also undergo dynamic instability. The increase in the extent of parallel overlap results in stronger shearing/accelerating effects, and thereby equalizes the velocities of all MTs in the same half-spindle, so the initially small differences in tubulin dimer velocities diminish fast in early anaphase B and do not play a significant role in the speckle velocity dispersal.

Estimates on pole-pole separation rate and the sliding motors' operating regime.

Here, to complement the numerical results obtained, we consider the oversimplified spindle (Fig. 3A), for which the corresponding force-balance and kinematic equations can be solved analytically. The system of three equations (1-3), describe the dynamics of the spindle poles and ipMTs. In this simplified configuration with N identical ipMT arrays composed of pairs of MTs emanating from the poles and overlapping antiparallel over a distance $L(t)$ at the equator, all MTs slide at the common rate $V_{sliding}(t)$ and we have

$$\text{(combining equations 1 and 3): } kNLF_m \left(1 - \frac{V_{sliding}}{V_m} \right) = \mu (V_{sliding} - V_{depoly}^-), \text{ where}$$

$(V_{sliding} - V_{depoly}^-)$ is the rate at which the poles diverge from the spindle equator, or

equivalently, half the rate of pole separation. Solving this force balance equation yields

$$\text{the sliding rate: } V_{sliding} = \frac{\alpha L}{1 + \alpha L} V_m + \frac{1}{1 + \alpha L} V_{depoly}^-, \text{ where } \alpha = \frac{kNF_m}{\mu V_m} \approx 10 / \mu m \text{ is an}$$

important parameter representing the ratio of the maximal motor generated force to the maximal viscous drag force per unit overlap length. If we assume that the ipMT overlap remains in the order of a micron (or few microns), αL is large (few tens), therefore

$$\frac{\alpha L}{1 + \alpha L} \sim 1 \text{ while } \frac{1}{1 + \alpha L} \sim 0, \text{ and consequently, sliding takes place at a rate almost equal}$$

to the 'free' sliding rate: $V_{sliding} \approx V_m$, indicating that motors operate against an almost

negligible resistance. This estimate, based on the assumption that an overlap in the order of a micron is maintained throughout anaphase B, illustrates how the sliding rate can

remain near its unloaded velocity in this rigid and idealized spindle geometry. If we also

assume that an overlap in the order of a micron is maintained throughout

metaphase/anaphase A, this estimate also predicts that the poleward flux rate in

metaphase/anaphase A is the same as half the rate of pole separation in anaphase B, $\approx V_m$, as observed (8). In addition, this estimate also illuminates how the overlap changes during anaphase B as long as it remains larger than or in the order of a micron. The overlap between antiparallel ipMTs decreases due to sliding, but increases due to mean net polymerization of the plus ends: $\frac{dL}{dt} = 2(V_{poly}^+ - V_{sliding})$. Therefore, as long as the overlap remains larger than or in the order of a micron, it changes at a rate $\approx 2(V_{poly}^+ - V_m)$ during anaphase B.

On the other hand, when L becomes small during the course of anaphase B, such that $\alpha L \ll 1$, then $\frac{\alpha L}{1 + \alpha L} \sim 0$ while $\frac{1}{1 + \alpha L} \sim 1$, and consequently $V_{sliding} \approx V_{depoly}^- = 0$, indicating that motors operate near stall, since the depolymerization is turned off at the onset of anaphase B (i.e. $V_{depoly}^- = 0$). The dynamics of the motors' transition from the unloaded regime to the stall regime is seen in Figure 4E (dotted-dash curve), where both the average depolymerization rate and the net polymerization rate are equal to zero, and pole separation is severely hindered (at $t \sim 20$ seconds) when the antiparallel overlap length decreases and fluctuates near zero (due to dynamic instability).

How do KLP3A motors regulate the switch from the metaphase/ anaphase A steady state to anaphase B?

We propose that KLP3A inhibition interferes with the suppression of flux by influencing the ratio of KLP10A motors to ipMT minus ends at the poles. In control spindles, KLP3A forms robust ipMT bundles which are “fed” into the poles. In pre-anaphase spindles these

ipMTs are depolymerized at the poles because the ratio of KLP10A to ipMT ends is high, but at anaphase B onset this ratio falls as KLP10A activity is inhibited. In KLP3A-inhibited embryos, ipMT bundles are less robust and the number of ipMT ends is lower, meaning that the actual ratio of residual KLP10A to ipMTs remains high even following anaphase B onset, and thus depolymerization and flux persist.

In the model results shown in Figure 4, we incorporated the effect of KLP3A inhibition directly as a reduction in the suppression of KLP10A-dependent depolymerization at anaphase B onset. Here, we investigate the above described mechanism for KLP3A action in our model, by incorporating the effect of KLP3A inhibition in anaphase B through a reduction in the number of ipMT arrays, a corresponding increase in viscous resistance per sliding motor, and a corresponding increase in the ipMT minus end depolymerization rate determined by the ratio of residual KLP10A molecules to ipMT minus ends. To determine the rate of depolymerization in KLP3A inhibited embryos with reduced numbers of ipMTs, we use a piecewise linear function between the number of active KLP10A motors per minus end and the mean depolymerization rate V_{depoly}^- (Fig. S2). Until the number of active KLP10A motors per minus end reaches the critical value, r_c , the mean depolymerization rate is zero, then, as the number of active KLP10A motors per minus end increases, the mean depolymerization rate increases linearly. When the ratio reaches the saturation level, r_s , the mean depolymerization reaches its maximal rate (the pre-anaphase B flux rate), which is limited either by sliding or by the number of motors that can fit onto the minus end, and remains at this maximal value despite further increases in the number of active KLP10A per minus end. This is the simplest function

which represents the mechanism described above. Based on previous studies on another MT depolymerase (9), we assume that, in this linear dependence, the maximal depolymerization rate is attained for $r_s \sim 10$, and $r_c \sim 1$. We further assume that in the control embryo, the ratio of active KLP10A number per minus end is greater than $r_s \sim 10$ during pre-anaphaseB, and is reduced to $r_c \sim 1$ at anaphase B onset when KLP10A is downregulated. In our model, we consider decreasing numbers of ipMTs (from $N = 40-4$), representing various degrees of the effect of KLP3A inhibitors. As shown in Figure S3, the results of these simulations are in good agreement with our experimental data on the flux-anaphase B relationship (Fig. 1C). In addition, our model results suggest that the experimental data on KLP3A inhibited embryos are best accounted for by spindles in which the number of ipMTs has been reduced significantly.

An alternative simple hypothesis that we considered in detail is that KLP3A motors simply change the effective outward force driving the poles apart, either by acting as ipMT sliding motors themselves or by augmenting the force generated by other ipMT sliding motors such as KLP61F (5). However, this alternative model does not explain the slope of the inverse linear relation between flux and spindle elongation (Fig. 1C) because a decrease in the outward force and sliding rate after KLP3A inhibition would result in lower rates of spindle elongation but would also decrease the flux rate. This is revealed by computer simulations of a model which assumes that KLP3A inhibition affects the number and efficacy of the force generators; this leads to a decrease in the rate of spindle elongation associated with a decrease in poleward flux rates (data not shown).

Another alternative hypothesis is that KLP3A motors might change the effective outward force driving the poles apart by augmenting the astral pulling forces. This possibility would explain the inverse linear relationship between the spindle elongation and the poleward flux rates but only if KLP10A driven depolymerization at the poles persists in anaphase B and the astral pulling rate in control embryos is exactly equal to the ipMT sliding rate (see below). However, this possibility was not further explored since ipMT sliding by KLP61F, and not astral pulling, is the prominent mechanism during the first half of anaphase B (11) and in addition, the KLP3A motors are localized in the interzone (10) and therefore are unlikely to act on astral MTs.

Fluctuations/ variance in anaphase B rate.

To analyze the variance in the anaphase B rate, let us first consider the simplified situation, in which two ipMT arrays composed of antiparallel MT pairs connect the spindle poles. The poleward fluxes and the mechanical characteristics of the motors sliding the two ipMT arrays differ. The first pair of MTs depolymerize at the poles with rate V_f^1 , while the second pair depolymerize with rate V_f^2 . Two Klp61F motors slide the respective pairs. The forces generated by the motors are $F_i = \zeta (V_s^i - V_m^i)$, $i = 1, 2$, where V_s^i are the sliding velocities, V_m^i are the free sliding motor rates, and ζ is the slope of the motors' linear force-velocity relation. The poles are separating with rate V_a , and the kinematic constraints on the rates of MT sliding, free motor sliding, and pole separation are: $2(V_s^1 - V_f^1) = 2(V_s^2 - V_f^2) = V_a$. In addition, the force balance equation in the regime where viscous resistance is negligible compared to motor forces is: $F_1 + F_2 \approx 0$. Solving

these three linear equations demonstrates that the average sliding rate is equal to the average free sliding motor rate, $\frac{V_s^1 + V_s^2}{2} = \frac{V_m^1 + V_m^2}{2}$ and that the anaphase B rate is given by

$$V_a = 2 \left(\frac{V_m^1 + V_m^2}{2} - \frac{V_f^1 + V_f^2}{2} \right).$$

In the general case, when there are many MT pairs

depolymerizing at the minus ends with variable rates and crosslinked by multiple sliding motors characterized by varying free sliding rates and force-velocity slopes, a similar analysis assuming independence of the variability of the number of motors per MT and other stochastic variables shows that the average sliding rate is equal to the average free sliding motor rate $\langle V_s \rangle = \langle V_m \rangle$, and the anaphase B rate is given by $V_a = 2(\langle V_m \rangle - \langle V_f \rangle)$.

This characterizes a single spindle and allows us to estimate the variance in the

$$\text{var}[V_a] = 4 \left(\frac{\text{var}[V_m]}{N_m} + \frac{\text{var}[V_f]}{N_{MT}} \right).$$

Here N_m is

the total number of motors, and N_{MT} is the total number of ipMT arrays in the spindle.

There is no direct data on the variance of the motor sliding rates, but assuming that it is of the same order as the observed variance of the motor sliding rates in *different* spindles,

then $\text{var}[V_m] \sim 10^{-3} \frac{\mu m^2}{\text{sec}^2}$. Using the available estimates of

$\text{var}[V_f] \sim 10^{-3} \frac{\mu m^2}{\text{sec}^2}$, $N_m \sim N_{MT} \sim 100$, we estimate that the standard deviation of the

anaphase B rate of a single spindle is very small, less than $0.01 \frac{\mu m}{\text{sec}}$, in agreement with

the law of large numbers (12). Such small fluctuations in the rate of pole separation

would not be detectable in our time lapse images. Indeed, linear fits to the pole-pole distance as a function of time of individual spindles are excellent.

Variance in speckle rates.

We undertook a quantitative analysis of the variance in flux rates because such analysis can potentially provide significant insights into the underlying mechanisms (13). Our analysis points to several sources of the observed variance, however, in our current data, the relationship between variance and mean in the flux rates is not convincing enough to make forceful conclusions about the source of the variance. In our model, we incorporated the factor which was pointed out to be most plausible as a result of the analysis below, and the variance in flux rates in our results (Fig. 4C,D) are in very good agreement with the experimental data (Fig. 1B,C).

Possible sources of the deviations in flux rates are first, velocity variance due to the motor-dependent “shearing”/“acceleration”, a consequence of parallel MTs within ipMTs (1, 4; Fig. 3D) however our analysis and computer simulations suggest that variance due to this factor is insufficient to explain the large variance observed and its contribution insignificant. Secondly, stochastic fluctuations in the elementary rate constants of mechanochemical coupling by the ipMT sliding motors (3, 4, 14) are another possible source of variance. Our analysis, including computer simulations, suggests that this factor’s contribution is significant, but it can not by itself explain the large dispersal in the flux rates.

A third source may be variance in the minus end depolymerization rate, which is the most plausible and provides the most significant contribution to the observed variance. The

variance in the depolymerization rate may, in turn, be influenced by several factors (15):

(i) One such factor is simple Poisson fluctuations in the number of subunits disassembled from the MT minus ends at the centrosome. If r is the average number of tubulin rings (tubulin dimers x 13) disassembled per second at the minus end, then the average

depolymerization rate is $\langle V_{flux} \rangle = \delta r$, where δ is the size of the tubulin dimer. The

variance in displacement is a linear function of time, and the variance of the rate

measured over time T is $\sigma_v = \frac{Var[X(T)]}{T^2} = \frac{\delta^2 r}{T}$ (16). Thus, with the average flux rate

over all inhibited and control spindles $\langle V_{flux} \rangle \sim 0.03 \frac{\mu m}{sec}$, $\delta = 0.008 \mu m$, and assuming

that a tubulin dimer remains in a speckle on average for a time $T \sim 5$ sec, the flux rate

variance due to Poisson fluctuations in the number of subunits dissembled would be

$\sim 10^{-4} \frac{\mu m^2}{sec^2}$, smaller, but of the same order of magnitude, as observed.

(ii) Finally, fluctuations in the number of KLP10A motors that depolymerize MT minus ends at the poles could also contribute to the observed variance in flux rates. If each

KLP10A motor induces depolymerization with constant rate v_{depoly} the total number of

working KLP10A motors is M and the number of minus ends is N , then the probability

that a motor will bind to a given MT is $p=1/N$. Then, the average number of motors per

minus end is $M/N=n$, and this number fluctuates according to the binomial distribution

(12) with variance $Mp(1-p)=M/N(1-(1/N)) \sim n$. Therefore, the average flux rate is nv_{depoly} ,

and its variance is nv_{depoly}^2 . In this case, the variance to flux ratio is equal to v_{depoly} . The

variance in measured flux velocities ranges from 0 to $0.0013 \mu\text{m}^2/\text{sec}^2$, with a mean value $\sigma_v \sim 0.0003 \mu\text{m}^2/\text{sec}^2$. Using this value and $\langle V_{flux} \rangle \sim 0.03 \mu\text{m}/\text{sec}$, we estimate $v_{depoly} \sim 0.01 \mu\text{m}/\text{sec}$.

Note, that this analysis predicts that the variance in flux is the increasing linear function of its mean: $\sigma_v = v_{depoly} \langle V_{flux} \rangle \approx 0.01 \langle V_{flux} \rangle$. We tested this prediction by plotting the experimentally measured variances in flux as a function of the mean flux rate, and found that the variance and the mean correlate linearly with coefficient ~ 0.006 of the same order of magnitude as the predicted coefficient ~ 0.01 . However, the statistical significance of this linear fit is not high enough to be confident in the numerical value of the slope, so further work is required to test this prediction and also to evaluate the influence of unavoidable experimental imprecision, for example in tracking the positions of moving speckles which could also contribute to the fluctuations in the observed flux rates.

In the simulations (all the figures and movies shown), we varied both the mean depolymerization and polymerization (growth and shrinkage) rates and their variances as follows. The variance of these rates, due to Poisson fluctuations in the number of dimers, is equal to $\sigma^2 = \delta(\text{mean rate})/2\tau$ over time τ . Correspondingly, at each computational time step, we displaced the minus and plus ends of the MTs by the distance

$\Delta x = \Delta t \cdot \sqrt{\sigma_c^2} \cdot \text{randn}$, where $\Delta t = 0.1$ is the time step (corresponding to 1 sec in real time), σ_c^2 is the corresponding computational value of the variance (0.01-0.1), and randn

is a random number generated by Matlab™ distributed according to the standard normal distribution.

To investigate the effect of stochastic fluctuations in the number of motors per unit length, the effective viscous drag coefficient, the maximal motor force and the free sliding motor velocity on the variance of flux rates, we varied them at each step according to the normal distributions with variances 10, 100 pN sec / μm , 1 pN and 0.03 $\mu\text{m}/\text{sec}$, respectively. Finally, we simulated individual tubulin dimers in different MTs moving poleward with varying rates, assumed that 10 or more fluorescent dimers correspond to a speckle (17), and compared trajectories of dimers and speckles. We found that the statistical behavior of the individual fluorescent dimers and of the speckles were the same.

Investigation of alternative mechanisms for anaphase spindle elongation.

We have addressed the feasibility of several alternative molecular mechanisms for anaphase B spindle elongation using computer simulations and/or evaluating their compatibility with previous experimental evidence.

1. Polymerization Ratchet

Could the outward force be generated by polymerizing MTs at the midzone rather than by the sliding action of KLP61F motors? The corresponding maximal force, namely hundreds of pN (a few pN per plus end (5)) would be sufficient, but the ‘free sliding’ rate

would be the polymerization rate, and such a model would predict that the anaphase B rate is proportional to the polymerization rate. However, since it is unclear what these MTs push against, we did not simulate this possibility.

2. Sliding against a spindle matrix

A second possibility is that the outward force is generated by KLP61F motors acting on ipMTs associated with a spindle matrix rather than by sliding antiparallel ipMTs (18). We have investigated this mechanism in a force-balance model. Under the assumption that KLP61F motors slide MTs against a hypothetical fixed spindle matrix, the forces, and thus the sliding velocities of MTs, depend on each one's overlap with the spindle matrix, and not on the anti-parallel overlap between MTs. The associated force-balance equations involving MTs' sliding velocities are similar to the ones described in our model. We have investigated the case of a fixed spindle matrix extending between the spindle poles, as well as a matrix within a limited region in the central spindle (Movie S1). In this model, a separate force-velocity relationship exists for each pole. MTs and motors in each half spindle develop a force and velocity depending on the number of MTs, matrix-MT overlaps, and viscous resistance of the corresponding pole, which, may well result in large fluctuations in pole-pole elongation rate. Thus, when the ipMTs slide against a fixed spindle matrix, as opposed to against one another, each pole would move independently at velocities related to their own molecular and biophysical parameters, which could potentially vary to a large extent (e.g. if one of the pole's movement is hindered the rate of poles separation could be reduced by half) and lead to large fluctuations in anaphase B velocity, which are not observed. However, in a symmetric

configuration (as in Movie S1) the poles move apart steadily and linearly, and our simulations show that this model could, in principle, explain all the data (in particular the data in Figure 1C), but it would not explain why KLP61F has evolved a bipolar structure.

3. Astral MTs pulling the poles

Finally, could motors at the cortex, for example dynein, generate the outward force by pulling on astral MTs? To investigate this mechanism, we simulated anaphase B spindle elongation by astral MT pulling, and we could recover the flux/anaphase B data in Figure 1C, under the following assumptions. (i) The rate of pulling of dynein-like motors on astral MTs is exactly equal to the sliding rate of the KLP61F motors in control embryos. (ii) KLP10A continues to depolymerize MT minus ends that are pushed into the poles by KLP61F-driven sliding throughout anaphase. (iii) MTs that do not have an antiparallel overlap are pulled apart with the poles, and KLP10A is inactive on these MTs.

We compute the sliding velocities of ipMTs similarly as in the other mechanisms, and anaphase spindle elongation in this case starts when dynein-like motors on astral MTs start pulling the poles apart (Movie S2). If we assume that KLP3A affects the pulling activity of dynein-like motors, and its inhibition leads to a reduction in the pulling rate, this model is able to explain the inverse relationship between the flux and anaphase B rates shown in Fig. 1C. However the assumption (i), particularly, seems unlikely, and this model cannot explain how inhibition of KLP61F on ipMTs has the observed effect of abolishing anaphase B (11).

Additional note on KLP10A driven depolymerization rate and the shortening rate of ipMT minus ends at the poles.

We assume that KLP10A motors remove tubulin subunits from the minus ends of ipMTs that are pushed by ipMT-MT sliding during pre-anaphase B. FSM of 10 μm long metaphase-anaphase A spindles reveals that tubulin speckles move away from the equator and towards the pole at $\sim 0.05 \mu\text{m/s}$ (Table 1). If we assume that the velocity of the speckles reflects the ipMT sliding rate, to maintain a steady state pole-pole spacing during pre-anaphase B, a shortening rate of ipMT minus ends must occur at $V_{\text{depoly}} = 0.05 \mu\text{m/s}$. This would imply that KLP10A motors must remove ~ 80 ($= 0.05 \mu\text{m/s} \times 1000 \times 8\text{nm} / 13$) tubulin subunits per second per MT at the poles. These estimates are in reasonable agreement with biochemical studies on KLP61F and KLP10A-related motors (7, 9).

References cited in Supporting Information:

1. Sharp, D.J., McDonald, K.L., Brown, H.M., Matthies, H.J., Walczak, C., Vale, R.D., Mitchison, T.J., & Scholey, J.M. (1999) *J. Cell Biol.* **144**, 125-138.
2. Sprague, B.L., Pearson, C.G., Maddox, P.S., Bloom, K.S., & Salmon, E.D. (2003) *Biophys. J.* **84**, 3529-3546.
3. Schnitzer, M.J., Visscher, K., & Block, S.M., (2000) *Nat. Cell Biol.* **2**, 718-723.
4. Mastrorarde, D.N., McDonald, K.L., Ding, R., & McIntosh, J.R. (1993) *J Cell Biol.* **123**, 1475-1489.
5. Cytrynbaum, E.N., Scholey, J.M., & Mogilner, A. (2003) *Biophys. J.* **84**, 757-769.

6. Rusan, N.M., Tulu, U.S., Fagerstrom, C., & Wadsworth, P. (2002) *J. Cell Biol.* **158**, 997-1003.
7. Cole, D.G., Saxton, W.M., Sheehan, K.B., & Scholey, J.M. (1994). *J. Biol. Chem.* **269**, 22913-22916.
8. Brust-Mascher, I., & Scholey, J.M. (2002) *Mol. Biol. Cell.* **13**, 3967-3975.
9. Hunter, A.W., Caplow, M., Coy, D.L., Hancock, W.O., Diez, S., Wordeman, L., & Howard, J (2003) *Mol. Cell.* **11**, 445-457.
10. Kwon, M., Mulia-Morales, S., Brust-Mascher, I., Sharp, D.J., Rogers, G.C., & Scholey, J.M. (2004) *Mol. Biol. Cell.* **15**, 219-233.
11. Sharp, D.J., Brown, H.M., Kwon, M., Rogers, G.C., Holland, G., & Scholey, J.M. (2000) *Mol. Biol. Cell.* **11**, 241-253.
12. Gardiner, C. (1985) Handbook of stochastic methods. Springer, New York.
13. Grill S.W., Howard, J., Schaffer, E., Stelzer, E.H., & Hyman, A.A. (2003) *Science.* **301**, 518-521.
14. Bianco P., Brewer, L.R., Corzett, M., Balhorn, R., Yeh, Y., Kowalczykowski, S.C., & Baskin, R.J. (2001) *Nature* **409**, 374-378.
15. Pedigo, S., & Williams, R.C. (2002) *Biophys J.* **83**, 1809-1819.
16. Mogilner, A., Elston, T., Wang, H-Y., & Oster, G. (2002) in *Computational Cell Biology*, eds. Fall, C.P., Marland, E., Tyson, J., & Wagner, J. (Springer, NY).
17. Waterman-Storer, C.M., & Salmon, E.D. (1998) *Biophys. J.* **75**, 2059-2069.
18. Kapoor, T.M., & Mitchison, T.J. (2001) *J. Cell Biol.* **154**, 1125-1133.

Figure Legends

Figure S1: The linear force-velocity relationship assumed for KLP61F motors.

Figure S2: Function depicting the relation between the average number of active KLP10A polymerases per minus end and the mean depolymerization rate of the minus end. r_c is the critical value of the average number of active KLP10A polymerases per minus end at which the mean depolymerization rate starts to deviate from zero, and r_s is the saturation level of this number beyond which no change in the depolymerization rate is observed.

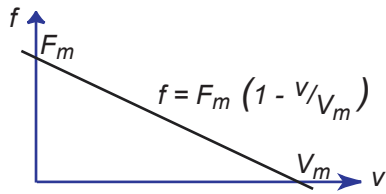
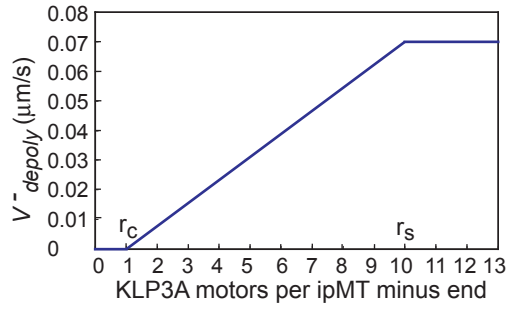
Figure S3: Numerical solutions of the poleward flux and spindle elongation rates in KLP3A inhibited spindles. The best fit to experimental data for KLP3A inhibited embryos (blue) is obtained when the number of ipMT arrays, N , is varied between 5 and 14 corresponding to high and low mean flux rates (orange). For each value of N , the corresponding depolymerization rate is calculated using the function in Figure S2, assuming $N = 40$ for control embryo. The model solutions (orange) are superimposed on the data from Figure 1C for KLP3A inhibited (blue) and control (grey) embryos. All other parameters are as in Table S1.

Movie Legends. The animations represent solutions to the appropriate model equations. Movie S1 represents the dynamics of ipMTs and the poles in the spindle matrix model for anaphase B. The yellow lines in the central spindle region represent an 8 μ m long spindle matrix against which KLP61F motors slide the MTs. The spindle elongates steadily despite the highly dynamic central region.

Movie S2 represents the dynamics of ipMTs and the poles in the astral pulling model for anaphase B. The green circles denote the position of the left and right spindle pole, which are being separated by dynein pulling the astral MTs (red arrowheads). The spindle elongates steadily as the poles are being separated, and the ipMTs are sliding apart freely by KLP61F motors, towards the moving poles.

Table S1: Model parameters.

Symbol	Meaning	Value	Ref.
Model parameters with little effect on the rate of early anaphase B			
F_m	Maximal motor force	1 pN	3
N	Number of overlapping arrays of ipMTs	30-90	1, 4
K	Number of motors per unit length	20/ μm	1
μ	Effective spindle viscous drag coefficient	1000pN·sec/ μm	5
V_{poly}^+	Mean ipMT plus end elongation rate	0.01-0.1 $\mu\text{m}/\text{sec}$	5
v_{growth}	ipMT plus end growth rate	0.16 $\mu\text{m}/\text{sec}$	6
v_{shrink}	ipMT plus end shrinkage rate	0.16 $\mu\text{m}/\text{sec}$	6
f_{rescue}	ipMT plus end rescue frequency	0.1-0.5 /sec	6
$f_{catastrophe}$	ipMT plus end catastrophe frequency	0.01-0.5 /sec	6
Model parameters which affect the rate of anaphase B			
V_m	Free sliding motor rate	0.07 $\mu\text{m}/\text{sec}$	7
V_{depoly}^-	ipMT minus end depolymerization rate	Variable (0-0.07 $\mu\text{m}/\text{sec}$)	

S1**S2****S3**